bioRxiv preprint doi: https://doi.org/10.1101/2023.03.06.531405; this version posted March 7, 2023. The copyright holder for this preprint (which was not certified by peer review) is the author/funder, who has granted bioRxiv a license to display the preprint in perpetuity. It is made available under aCC-BY-NC 4.0 International license.

Cell-Type Specific Connectivity of Whisker-Related Sensory and Motor Cortical Input to Dorsal Striatum

Abbreviated Title: Differential connectivity of sensory and motor corticostriatal inputs

Authors: Branden D. Sanabria[1], Sindhuja S. Baskar[1], Alex J. Yonk[1], Christian R. Lee[1], and David J. Margolis[1,2]

[1]Department of Cell Biology and Neuroscience, Rutgers, The State University of New Jersey, 604 Allison Road, Piscataway, NJ, 08854, USA

[2]Lead contact

Correspondence to: David J. Margolis, Ph.D.

david.margolis@rutgers.edu

Number of Pages: 41

Number of figures: 6

Number of tables: 1

Number of words in abstract (240), introduction (567), discussion (1562)

Acknowledgements

This work was funded by the National Institutes of Health (NIH F31 NS124343) (NIH R01NS094450) and the National Science Foundation (NSF IOS-1845355)

Conflicts of interest statement

The authors declare no competing financial interest.

bioRxiv preprint doi: https://doi.org/10.1101/2023.03.06.531405; this version posted March 7, 2023. The copyright holder for this preprint (which was not certified by peer review) is the author/funder, who has granted bioRxiv a license to display the preprint in perpetuity. It is made available under aCC-BY-NC 4.0 International license.

Abstract:

The anterior dorsolateral striatum (DLS) is heavily innervated by convergent excitatory projections from the primary motor (M1) and sensory cortex (S1) and is considered an important site of sensorimotor integration. M1 and S1 corticostriatal synapses have functional differences in the strength of their connections with striatal spiny projection neurons (SPNs) and fast-spiking interneurons (FSIs) in the DLS, and as a result exert an opposing influence on sensory-guided behaviors. In the present study, we tested whether M1 and S1 inputs exhibit differences in the subcellular anatomical distribution onto striatal neurons. We injected adeno-associated viral vectors encoding spaghetti monster fluorescent proteins (sm.FPs) into M1 and S1, and used confocal microscopy to generate 3D reconstructions of corticostriatal inputs to single identified SPNs and FSIs obtained through ex-vivo patch-clamp electrophysiology. We found that SPNs are less innervated by S1 compared to M1, but FSIs receive a similar number of inputs from both M1 and S1. In addition, M1 and S1 inputs were distributed similarly across the proximal, medial, and distal regions of SPNs and FSIs. Notably, clusters of inputs were prevalent in SPNs but not FSIs. Our results suggest that SPNs have stronger functional connectivity to M1 compared to S1 due to a higher density of synaptic inputs. The clustering of M1 and S1 inputs onto SPNs but not FSIs suggest that cortical inputs are integrated through cell-type specific mechanisms and more generally have implications for how sensorimotor integration is performed in the striatum.

Significance Statement:

The dorsolateral striatum (DLS) is a key brain area involved in sensorimotor integration due to its dense innervation by the primary motor (M1) and sensory cortex (S1). However, the quantity and anatomical distribution of these inputs to the striatal cell population has not been well characterized. In this study we demonstrate that corticostriatal projections from M1 and S1

bioRxiv preprint doi: https://doi.org/10.1101/2023.03.06.531405; this version posted March 7, 2023. The copyright holder for this preprint (which was not certified by peer review) is the author/funder, who has granted bioRxiv a license to display the preprint in perpetuity. It is made available under aCC-BY-NC 4.0 International license.

differentially innervate spiny projection neurons (SPNs) and fast-spiking interneurons (FSIs) in the DLS. S1 inputs innervate SPNs less than M1 and are likely to form synaptic clusters in SPNs but not in FSIs. These findings suggest that sensorimotor integration is partly achieved by differences in the synaptic organization of corticostriatal inputs to local striatal microcircuits.

Introduction

Sensorimotor integration is the ability to identify important stimuli from the environment and use this information to guide behaviors essential for survival (Machado et al, 2010). Neurons in the primary motor (M1) and primary sensory (S1) cortices play a role in this process by sending excitatory glutamatergic projections to the striatum, a subcortical region, and the main input nucleus of the basal ganglia network (Hoffer & Alloway, 2001). Generally, cortical projections from functionally related brain regions show higher density and significant overlap amongst their projection fields in the striatum (Bolam et al, 2002; Hintiryan et al, 2016; Hunnicutt et al, 2016). Notably, the dorsolateral striatum (DLS) is a site of overlap between inputs from M1 and S1 and plays a critical role in sensorimotor integration (Hoffer & Alloway, 2001; Hunnicutt et al, 2016; Makino et al, 2016; Hooks et al, 2018; Smith et al, 2022), but how these inputs are integrated by different cell types in DLS is still unclear.

The DLS mostly contains inhibitory GABAergic spiny projection neurons (SPNs) and a sparse population of various interneurons (Kawaguchi, 1993 & 1997; Tepper et al, 2018). Activation of SPNs that express the D1 dopamine receptor constitute the “direct” pathway and promote selected motor actions, while SPNs that express the D2 dopamine receptor constitute the “indirect” pathway and inhibit non selected motor actions (Kreitzer & Malenka, 2008). One major interneuron type, the parvalbumin-positive fast spiking interneuron (FSI), is a potent inhibitor of striatal SPNs and involved in sensorimotor transformation of behavior (Lee et al, 2019; Gritton et

bioRxiv preprint doi: https://doi.org/10.1101/2023.03.06.531405; this version posted March 7, 2023. The copyright holder for this preprint (which was not certified by peer review) is the author/funder, who has granted bioRxiv a license to display the preprint in perpetuity. It is made available under aCC-BY-NC 4.0 International license.

al, 2019; Martiros et al, 2019). For example, stimulation of S1 inputs to FSIs in the DLS suppresses responding to both rewarded and unrewarded cues in a whisker-based texture discrimination task. In contrast, stimulation of the M1 inputs, which has a different balance of functional innervation to SPNs compared to S1, promotes behavioral responses in the same task (Lee et al, 2019). SPNs and FSIs rely on excitatory inputs along the extent of their elaborate dendrites to drive action potential discharge (Kawaguchi, 1993 & 1997; Stern et al, 1998; Tepper et al, 2018). Therefore, both the local connectivity and external synaptic inputs are important factors of integration in the DLS (Straub et al, 2016; Hjorth et al, 2020).

While M1 and S1 inputs are capable of evoking excitatory postsynaptic potentials (EPSPs) in SPNs and FSIs, recent reports have found that S1 inputs generate larger responses in FSIs compared to SPNs (Lee et al, 2019; Johansson & Silberberg, 2020). Conversely, Lee et al. (2019) found that the response to stimulation of M1 inputs was similar for SPNs and FSIs. Potential differences in synaptic efficacy of M1 and S1 corticostriatal inputs to striatal neurons could reflect presynaptic, postsynaptic, or structural differences (Fino et al, 2005; Perrin & Venance, 2019; Badreddine et al, 2022), mechanisms that could interact to produce differences in functional innervation. Two properties that have been associated with the efficacy of total synaptic input that a cell receives are the number of synaptic inputs and the distribution of synapses along the dendritic arbor (Rall, 1967; Magee, 2000). Understanding how M1 and S1 inputs are organized onto SPNs and FSIs can reveal how the DLS integrates functionally related signals and commands downstream basal ganglia nuclei, which ultimately affect behavior. Here, we investigate the structural input to SPNs and FSIs and provide evidence for the differential innervation of striatal neurons by M1 and S1.

bioRxiv preprint doi: https://doi.org/10.1101/2023.03.06.531405; this version posted March 7, 2023. The copyright holder for this preprint (which was not certified by peer review) is the author/funder, who has granted bioRxiv a license to display the preprint in perpetuity. It is made available under aCC-BY-NC 4.0 International license.

Materials and Methods:

Animals

All procedures involving animals were approved by the Rutgers University Institutional Animal Care and Use Committee (Protocol #: 999900197). Experiments were performed on wild-type male and female mice on a C57BL/6J background of at least 3 months of age at the time of the first surgical procedures. Mice were housed in a reverse light cycle room (lights off from 08:00 to 20:00) with food and water available *ad libitum*. All mice underwent two simultaneous unilateral Adeno Associated Virus (AAV) injections between 35 and 104 days old and all mice were euthanized after at least three weeks post injection.

Viral injection

Briefly, mice were anesthetized with isoflurane (4% induction, 0.8%–1.5% maintenance) and placed onto a stereotaxic frame (Kopf) with a feedback-controlled heating blanket maintained at ~36°C (FHC). Rimadyl (5 mg/kg; Hospira) and Bupivacaine (0.25%, 0.1 mL; Fresenius Kabi) were injected subcutaneously into the left flank and scalp, respectively. The scalp was cleaned with Betadine (Purdue Products) followed by 70% ethanol three times. A midline incision was made, and the skull was exposed and leveled relative to bregma and lambda in the dorsoventral plane. A craniotomy was made above both injection sites, and ~270 nL of pAAV.CAG.Flex.Ruby2sm-Flag.WPRE.SV40 (#98928; Addgene), pENN.AAV.CAG.Flex.GFPsm_myc.WPRE.SV40 (#98927; Addgene) mixed 1:1 with pAAV.CAMKII.Cre.SV40 (#105558; Addgene), or pAAV.CAG.GFPsm-myc.WPRE.SV40 (#98926; Addgene) diluted 1:1 in 0.1M PBS were pressure injected into either left whisker M1 (anteroposterior (AP): +1.6mm, mediolateral (ML): +1.5mm, dorsoventral (DV): -0.6mm) or left whisker S1 (AP: -1.0mm, ML: +3.3mm, DV: -0.6mm) via a glass micropipette (BlueBrand IntraMark) over the course of 5 minutes followed by another 5 minute delay to permit viral

bioRxiv preprint doi: https://doi.org/10.1101/2023.03.06.531405; this version posted March 7, 2023. The copyright holder for this preprint (which was not certified by peer review) is the author/funder, who has granted bioRxiv a license to display the preprint in perpetuity. It is made available under aCC-BY-NC 4.0 International license.

diffusion. After the micropipette was slowly raised, the scalp was closed and secured with sutures and tissue glue. After surgery, mice were placed in clean, temporary housing and monitored for 72 hours. After this monitoring period, mice were transferred to their home cages and allowed to recover for at least 3 weeks to allow for viral expression to fully label neuronal processes.

Whole cell patch clamp recordings

Mice were induced with 3% isoflurane, deeply anesthetized with ketamine-xylazine (300/30 mg/kg), and transcardially perfused with recovery artificial cerebrospinal fluid (ACSF) containing 103mM NMDG, 2.5mM KCl, 1.2mM NaH_2PO_4, 30mM $NaHCO_3$, 20mM HEPES, 25mM Glucose, 101mM HCl (1N), 10mM $MgSO_4$, 2mM Thiourea, 3mM Sodium Pyruvate, 12mM N-Acetyl-L-Cysteine, and 0.5mM $CaCl_2$ (saturated with 95% O_2 and 5% CO_2). After decapitation and extraction, the brain was glued to a vibratome stage, immersed in RT oxygenated recovery ACSF, and 300µm coronal sections were cut using a Leica VT1200S vibratome. Sections were immediately transferred to the same oxygenated medium at 35°C for ~5 min, after which they were transferred to oxygenated external ACSF containing 124mM NaCl, 2.5mM KCl, 26mM $NaHCO_3$, 1.2mM NaH_2PO_4, 10mM Glucose, 3mM Sodium Pyruvate, 1mM $MgCl_2$, and 2mM $CaCl_2$ at RT for at least 1 hour before use.

Whole-cell patch clamp recordings were obtained in a chamber that was constantly perfused (2-4 ml/min) with oxygenated external ACSF at 34°C. Sections and neurons were visualized using infrared differential interference contrast (IR-DIC) microscopy with a IR1000 CCD camera (Dage-MTI) mounted onto an BX51-WI upright microscope (Olympus) fitted with two switchable lenses: a 4X air lens and a 40X water-immersion lens. Patch pipettes (2-5MΩ) were fabricated by pulling borosilicate glass micropipettes (2mm o.d., Warner Instruments) via a P-1000 horizontal puller (Sutter Instruments). The internal pipette solution contained 130mM K

bioRxiv preprint doi: https://doi.org/10.1101/2023.03.06.531405; this version posted March 7, 2023. The copyright holder for this preprint (which was not certified by peer review) is the author/funder, who has granted bioRxiv a license to display the preprint in perpetuity. It is made available under aCC-BY-NC 4.0 International license.

methanesulfonate, 10mM KCl, 10mM HEPES, 2mM $MgCl_2$, 4mM Na_2ATP, 0.4mM Na_2GTP at pH 7.25 and 290-295mOsm/L. In addition, 2% biocytin was freshly dissolved in the internal solution on each recording day. Current clamp recordings were obtained from neurons within the anterior dorsal striatum (approximately 1.4 to 0.4mm relative to bregma). Once a selected cell was patched, it was subjected to hyperpolarizing and depolarizing current steps (-500pA to 500pA, 100pA steps, 500ms, 11 sweeps) for post-hoc electrophysiological analysis and identification. Additionally, patched neurons were held for at least 15 minutes to permit biocytin filling for post-hoc morphological analysis and identification. Data were acquired via a HEKA EPC10USB amplifier and digitized at 20kHz in Patchmaster Next (HEKA). We did not correct for the liquid junction potential.

Analysis of patch clamp recordings

Analysis of electrophysiological responses to hyperpolarizing and depolarizing current injections were performed using MATLAB and Python. In MATLAB, a custom script was used to import (Keine, 2022), standardize, and save the data as a .mat variable. A custom python script was used to import and analyze the data stored in the mat variable, partly using the electrophysiology feature extraction library (eFEL) (Van Geit et al., 2016) of the Blue Brain Project (Blue Brain Project, 2015). Briefly, eFEL was used to mark specific sweep events including the values and indices of action potential (AP) thresholds, peaks, and after hyperpolarizations (AHP) to calculate physiological parameters including half-height width, interspike interval, instantaneous firing frequency, and max firing frequency. The half-height width (HHW) of each AP (from AP threshold to AHP) was calculated by setting half the maximum amplitude ((Peak value - AP threshold value) / 2) as a horizontal threshold, interpolating a line containing 1000 points over the AP, identifying when the interpolated line crossed the threshold

bioRxiv preprint doi: https://doi.org/10.1101/2023.03.06.531405; this version posted March 7, 2023. The copyright holder for this preprint (which was not certified by peer review) is the author/funder, who has granted bioRxiv a license to display the preprint in perpetuity. It is made available under aCC-BY-NC 4.0 International license.

during the rising and falling phases, and subtracting the values from each other. The interspike interval (ISI) was calculated by subtracting the latter AP threshold value from the former (e.g., ISI[i] = APthres[i+1] - APthres[i]). The instantaneous firing frequency (IFF) was calculated by dividing the interspike interval values by 1 (e.g., IFF = 1/ISI). The max firing frequency was calculated by selecting the maximum frequency value (e.g., MFF = max (IFF)).

Immunohistochemistry

After patch clamp recordings, ex vivo slices were stored in 4% PFA overnight. Free-floating sections were washed in 0.1M PBS and incubated with 1% NaBH4 for 20 minutes, washed again, and then incubated with 10% MeOH + 3% H2O2 for 15 minutes. Slices were then incubated in blocking buffer (5% NGS + 2% BSA + 0.5% triton X-100) for 1 hour at RT followed by overnight incubations of 1^{o} antibodies (Chk α-GFP (1:1000) Rockland 600-901-215; Rb α-FLAG (1:1000) Sigma F7425) diluted in blocking buffer at RT. The following day, slices were washed with 0.1M PBS and incubated with 2^{o} antibodies (Streptavidin-Cy5 (1:300) Jackson Immunoresearch 016-170-084; Goat α-Chk 488 (1:500) ThermoFisher Scientific A-11039; Goat α-Rb 594 (1:500) ThermoFisher Scientific A-11037) for 4 hours at RT. Slices were washed with PBS, mounted onto slides (ThermoFisher Scientific 12-550-15) via Aquamount (ThermoFisher Scientific, 13800) and cover-slipped (ThermoFisher Scientific 12-540-B) before imaging. For one FSI slice, we tested a fast-optical clearing method (FOCM) because it has been shown to enhance the imaging of fine structures, such as synaptic contacts, in thick sections with minimal loss of endogenous fluorescence and tissue distortion in mice (Zhu et al, 2019). We did not observe any significant distortion to the tissue or morphology of our biocytin filled neuron using this method and this cell was included in the analysis.

Confocal imaging

bioRxiv preprint doi: https://doi.org/10.1101/2023.03.06.531405; this version posted March 7, 2023. The copyright holder for this preprint (which was not certified by peer review) is the author/funder, who has granted bioRxiv a license to display the preprint in perpetuity. It is made available under aCC-BY-NC 4.0 International license.

Confocal Z-stack images were obtained using a Zeiss LSM 800 confocal microscope. Fixed slices containing filled neurons from ex vivo recordings were imaged using a 40x oil immersion objective (Plan-Apochromat 40x/1.4 Oil DIC (UV) VIS-IR M27) set at 1.0 airy disk unit. The biocytin filled cell was centered in the field of view, and the zoom factor was set to a minimum of 0.5x or adjusted to capture the entirety of the dendritic field. Images acquired at either 1024 x 1024 or 2048 x 2048 pixels with a 0.5x zoom factor corresponded to a minimum voxel dimension of 0.312 x 0.312 x 0.530 µm or 0.156 x 0.156 x 0.530 µm respectively in the X, Y, and Z dimensions. Fluorescence acquisition settings were as follows: Alexa Fluor 488 (excitation 493λ, emission 517λ, detection 490–550λ), Alexa Fluor 568 (excitation 577λ, emission 603λ, detection 565–642λ), Alexa Fluor 647 (excitation 653λ, emission 668λ, detection 645–700λ). The pinhole size of the objective was set to 1.0 airy disk unit when capturing the longest wavelength fluorophore (Alexa Fluor 647). When imaging the other fluorophores (Alexa Fluor 405, 488, and 568), the pinhole size was adjusted to match the airy disk size of the 647 laser. This ensured that the scan with each laser excited fluorophores in the same sized area. Optical laser intensities were set individually for each channel and optimized throughout the Z-stack using the Z-stack auto-brightness correction tool. Z-stack ranges were set manually by tracking the range of the entire labeled cell.

Morphological measurements

For each neuron in our dataset, we obtained the position along the AP, ML, and DV axes by manually aligning the coronal field view of the recorded slice with the corresponding Allen brain atlas figure (Allen Reference Atlas). We were not able to obtain the ML and AP position for one SPN and one FSI. Dendritic field measurements were obtained by creating a 2D orthogonal projection of the confocal Z-stack and then measuring the largest diameter of an elliptical sphere

bioRxiv preprint doi: https://doi.org/10.1101/2023.03.06.531405; this version posted March 7, 2023. The copyright holder for this preprint (which was not certified by peer review) is the author/funder, who has granted bioRxiv a license to display the preprint in perpetuity. It is made available under aCC-BY-NC 4.0 International license.

205 encompassing the neuron using ImageJ (Fiji) software. The range along the Z-axis for each cell
206 was calculated as the distance between the first and last appearance of neuronal processes in the
207 Z-stack.

208 **Imaris 3D-reconstructions of single neurons**

209 Carl Zeiss image files were imported into Imaris version 9.7 equipped with the Filament
210 Tracer plugin (Bitplane). Biocytin filled neurons were first reconstructed into 3D-surface objects
211 using the "surfaces" tool. For our surface reconstructions, the "background subtraction" option
212 was enabled and the "smoothing" option was disabled to avoid adding artificial curvature to the
213 cell (Fogarty et al, 2013). We determined the largest diameter setting by measuring the largest
214 cross-sectional diameter of the soma in the "slice view" mode. Using an interactive histogram of
215 volumetric pixels, we manually adjusted the threshold to include as much of the neuron as possible
216 while aiming to exclude any extraneous background fluorescence. Neurons were then
217 reconstructed using the "filament tracer" plugin using a semi-automated tracing method.
218 Reconstructing the neuron as a filament allowed us to segment the neuron into separate branch
219 levels and dendrites, as well as obtain distance measurements for M1 and S1 inputs from the
220 beginning of the filament (soma). To construct the neuron as a "filament" we manually traced the
221 dendrites using the "autopath" tool. Once the final outline of the neuron was created, the diameter
222 of the dendrites was adjusted using an automatic threshold. For SPNs, we used the automatic spine
223 detection tool in the "filament" tab to detect and reconstruct dendritic spines. The diameter and
224 length of spines were measured in "slice viewer" using min/max diameters of 0.6 μm and 2.5 μm
225 for automatic spine detection thresholds. This step was excluded for our FSI dataset due to the lack
226 of spines on their dendrites. We verified that there was a single filament for each reconstruction

bioRxiv preprint doi: https://doi.org/10.1101/2023.03.06.531405; this version posted March 7, 2023. The copyright holder for this preprint (which was not certified by peer review) is the author/funder, who has granted bioRxiv a license to display the preprint in perpetuity. It is made available under aCC-BY-NC 4.0 International license.

and that all the branch points and dendrites were accurately represented in comparison to the raw fluorescence images.

M1 and S1 corticostriatal synaptic puncta identification and quantification

The Imaris "surface" reconstruction enabled us to mask the raw fluorescence from M1 and S1 channels onto the neuron. Using the "edit" tab within the surface reconstructed neuron, we masked putative presynaptic contacts from M1 and S1 corticostriatal projections by setting the intensity of voxels outside of the surface to 0. This allowed us to filter putative presynaptic contacts so that only fluorescence from M1 and S1 that colocalized with the surface reconstruction remained. This step resulted in two new fluorescent channels representing masked fluorescence from M1 and S1 onto the neuron.

Fluorescence from masked M1 and S1 inputs were made into 3-D spots using the "spots" tool. First, the cross-sectional diameter of putative presynaptic puncta from cortical projections was measured in "slice viewer". The "different spot sizes" option was checked because fluorescent puncta from M1 and S1 varied in size. We chose a minimum diameter of 1µm and the "background subtraction" option was disabled. Spots were manually thresholded using an interactive histogram and then validated by verifying that the new spot object was representing masked fluorescence from a corticostriatal projection and not from extraneous background fluorescence. The "spots region type" was set to "local contrast" and the "spots regions" diameter threshold was set to "region border". We used automatic thresholds for these two parameters and found that they gave us the best representation of our puncta as 3D-objects.

In Imaris, the default "spots close to filament" function is capable of filtering and quantifying M1 and S1 spots whose center lies within a specified distance from the edge of a neuron reconstructed as a filament object. However, it was limited in that it provided us with the

bioRxiv preprint doi: https://doi.org/10.1101/2023.03.06.531405; this version posted March 7, 2023. The copyright holder for this preprint (which was not certified by peer review) is the author/funder, who has granted bioRxiv a license to display the preprint in perpetuity. It is made available under aCC-BY-NC 4.0 International license.

absolute distance of each spot from the soma instead of considering the length of the dendrites. To circumvent this issue, we used a publicly available custom python script provided by Dr. Matthew Gastinger (Gastinger, 2022). Using the "spots close to filament" function provided by this script, we filtered S1 and M1 spots so that only those with edges were within 0.5 µm from the edge of the filament-constructed neuron remained, and we identified these spots as putative M1 and S1 inputs. This custom script also provided us with the quantity of inputs and the distance from the soma measured along the dendrite for each spot object.

Statistical analyses

All statistical analyses were performed using GraphPad Prism software. For each metric, we first tested if the data was normally distributed using the Shapiro-Wilk test (Ghasemi & Zahediasl, 2012; Mishra et al, 2019). For normally distributed data, parametric comparative t-tests were used. A statistical F-test was first used to compare variances between groups. If the standard deviation between two normally distributed data sets was significantly different, the unequal variance Welch's t-test was used. For unpaired samples that were not normally distributed the nonparametric Mann-Whitney U test was used. For paired data that was not normally distributed we used the Wilcoxon matched pairs signed rank test. For multiple group comparisons, we used the analysis of variance (ANOVA) statistical test. All data are presented as the mean +/- SEM.

Code accessibility

A custom Imaris extension written and provided by Dr. Matthew Gastinger is publicly available through Github (Gastinger, 2022). Scripts used for the analysis of the electrophysiological recordings are available through the Margolis Github. (https://github.com/margolislab)

bioRxiv preprint doi: https://doi.org/10.1101/2023.03.06.531405; this version posted March 7, 2023. The copyright holder for this preprint (which was not certified by peer review) is the author/funder, who has granted bioRxiv a license to display the preprint in perpetuity. It is made available under aCC-BY-NC 4.0 International license.

Results:

M1 and S1 corticostriatal projections converge in the dorsolateral striatum

We injected adeno associated viruses (AAVs) encoding spaghetti monster fluorescent proteins (sm.FPs) GFP or Ruby into whisker M1 and whisker S1 to observe putative synaptic contacts onto striatal neurons via confocal light microscopy. We used sm.FPs because of their utility in multicolor experiments, enhanced fluorescence, and better resolution when imaging fine structures such as synaptic terminals (Viswanathan et al, 2015). To ensure there was no bias in the expression of sm.FPs due to the injection site, we counterbalanced the injection of sm.FPs in M1 and S1 throughout the experiments. In total, 7 mice were injected with sm.FP-GFP in S1 and sm.FP-Ruby in M1, and 3 mice were injected with sm.FP-GFP in M1 and sm.FP-Ruby in S1.

After waiting at least 3 weeks to permit viral expression, coronal slices containing the anterior striatum were obtained. Ex-vivo whole-cell patch clamp recordings were performed ipsilateral to the injection site to characterize the electrophysiological properties and fill individual neurons with biocytin (Fig 1A). Recorded and filled neurons were located within extensively overlapping sm.FP-labeled M1 and S1 corticostriatal projections in the dorsolateral region of the striatum (DLS) (Fig. 1B). Our final data set includes 14 striatal neurons from 10 mice (2 males, 8 females). 13 additional cells from 6 mice were excluded from reconstruction and analysis due to incomplete biocytin cell fills, inconclusive immunohistochemistry containing artifacts, excessive background fluorescence, or the inability to be identified as an SPN or FSI via their morphology or electrophysiology.

Patched SPNs and FSIs are identified by their distinct morphological and electrophysiological properties

bioRxiv preprint doi: https://doi.org/10.1101/2023.03.06.531405; this version posted March 7, 2023. The copyright holder for this preprint (which was not certified by peer review) is the author/funder, who has granted bioRxiv a license to display the preprint in perpetuity. It is made available under aCC-BY-NC 4.0 International license.

Striatal neurons were patched without the use of genetic cell identification due to the expression of sm.FPs GFP and Ruby in cortical inputs, which limited our ability to record from SPNs or FSIs labeled with fluorescent markers such as GFP or TdTomato. Instead, patched striatal neurons were identified by their morphological and electrophysiological features, as in previous studies (Kawaguchi, 1993 & 1997; Tepper et al, 2018). We identified two distinct populations of striatal neurons in our dataset. Since 95% of the striatal population consist of SPNs, there was a high probability of patching them relative to FSIs (Hjorth et al, 2020). These experiments did not distinguish between D1- and D2-SPNs.

Most of the population (N= 9 cells) was identified as SPNs primarily based on the presence of prominent spines embedded along the dendrites (Fig. 1C). In comparison, a second population (N= 5 cells), identified as FSIs, often contained a fusiform-shaped soma, frequently branched, varicose aspiny dendrites, and dense axonal arborizations surrounding the dendritic field (Fig. 1C). We found no significant differences in the maximum size of the dendritic field (SPN = 284.6 +/- 12.39µm, N = 9 vs FSI = 269.1 +/- 24.52µm, N = 5, p = 0.539, t = 0.6323, df = 12, unpaired two tailed t-test) (Fig. 1-1a) or the range of the dendrites along the Z-axis between the two groups of neurons (SPN = 73.81 +/- 8.974µm, N = 9 vs FSI = 80.34 +/- 12.38µm, N = 5 p = 0.6748, t = 0.4301, df = 12, unpaired two tailed t-test) (Fig. 1-1b). However, SPNs had significantly fewer primary dendritic branches (SPN = 4.88 +/- 0.3889, N = 9 vs FSI = 7.6 +/- 1.166, N = 5, p = 0.0183, t = 2.728, df = 12, unpaired two tailed t-test) and slightly smaller soma diameter compared to FSIs (SPN = 14.26 +/- 0.4528µm, N = 9 vs FSI = 16.98 +/- 1.389µm, N = 5, p = 0.1228, t = 1.865, df = 7.206, unequal variance Welch's t-test) (Fig. 1D), which is similar to what has been previously reported (Kawaguchi, 1993 & 1997; Fino & Venance, 2011; Tepper et al, 2018).

bioRxiv preprint doi: https://doi.org/10.1101/2023.03.06.531405; this version posted March 7, 2023. The copyright holder for this preprint (which was not certified by peer review) is the author/funder, who has granted bioRxiv a license to display the preprint in perpetuity. It is made available under aCC-BY-NC 4.0 International license.

FSIs are characterized by their higher frequency (up to 100 Hz) action potential firing and shorter action potential duration, thus we could compare the mean instantaneous frequency and the mean half-height width of action potentials evoked in current clamp recordings to distinguish them from other types of aspiny neurons in the striatum (Kawaguchi, 1993 & 1997; Tepper et al, 2018) (Fig. 1E). The subpopulation of aspiny neurons identified as FSIs had shorter mean half-height widths (FSI_{HHW} = 0.40 +/- 0.04 ms, N = 5 vs SPN_{HHW} = 1.21 +/- 0.13 ms, n = 8, p = 0.0016, Mann-Whitney U = 0) (Fig. 1E, 1-1c), faster mean instantaneous firing frequencies (FSI_{IFF} = 76.84 +/- 3.56 Hz, N = 5 vs SPN_{IFF} = 26.99 +/- 3.07 Hz, n = 8, p < 0.0001, t = 10.38, df = 11, unpaired two tailed t-test) (Fig. 1E, 1-1d), more depolarized resting membrane potentials (FSI_{RMP} = -64.69 +/- 0.960 mV, N = 5 vs SPN_{RMP} = -74.16 +/- 1.787 mV, n = 8 vs, p = 0.0024, t = 3.924, df = 11, unpaired two tailed t-test) (Fig. 1-1e), faster maximal firing frequencies (FSI_{MFF} = 102.3 +/- 7.348 Hz, N = 5 vs SPN_{MFF} = 37.02 +/- 5.146 Hz, n = 8, p < 0.0001, t = 7.505, df = 11, unpaired two tailed t-test) (Fig. 1F), and shorter interspike intervals (FSI_{ISI} = 13.27 +/- 0.6246 ms, N = 5 vs SPN = 41.68 +/- 5.137 Hz, n = 8, p = 0.0008, t = 5.490, df = 7.206, unequal variance Welch's t-test) (Fig. 1F) compared to SPNs.

SPNs and FSIs had similar input resistances ($FSI_{Input\ Resistance}$ = 114.0 +/- 8.513 MΩ, N = 5 vs $SPN_{Input\ Resistance}$ = 126.6 +/- 18.65 MΩ, n = 8, p = 0.6217, t = 0.5077, df = 11, unpaired two tailed t-test) (Fig. 1-1f). One neuron did not reach steady state firing during patch clamp recordings and was excluded from the analysis of ephys parameters but was still included in the SPN group based on its dendritic morphology.

To verify that there were no differences in the recording site within the striatum for SPNs and FSIs, we determined the position of the recorded cell relative to the anatomical features of the slice for a subset of neurons. Most neurons were obtained in the dorsal aspect of the striatum where

bioRxiv preprint doi: https://doi.org/10.1101/2023.03.06.531405; this version posted March 7, 2023. The copyright holder for this preprint (which was not certified by peer review) is the author/funder, who has granted bioRxiv a license to display the preprint in perpetuity. It is made available under aCC-BY-NC 4.0 International license.

M1 and S1 corticostriatal projections were concentrated and there were no significant differences in the recording location for both types of neurons (SPN_{ML} = + 1.738 +/- 0.059, n = 8 vs FSI_{ML} = +1.700 +/- 0.2245mm, n = 4, p = 0.8808, t = 0.1614, df = 3.430, unequal variance Welch's t-test; SPN_{AP} = + 1.120 +/- 0.0414, n = 8 vs FSI_{AP} = + 1.040 +/- 0.1249, n = 4, p = 0.4555, t = 0.7763, df = 10, unpaired two tailed t-test; SPN_{DV} = -2.265 +/- 0.1101, n = 8 vs FSI_{DV} = -2.125 +/- 0.1199, n= 4, p = 0.4516, t = 0.7833, df = 10, unpaired two tailed t-test) (Fig. 1G) (Table 1).

Overall, the neurons in our dataset have morphological and electrophysiological properties that are consistent with the well-documented differences between SPNs and FSIs. Using the absence of spines on the dendrites and the presence of fast spiking enabled us to differentiate between FSIs and SPNs without the use of genetically encoded fluorescent markers, such as parvalbumin, which is commonly used to label FSIs (Kawaguchi, 1993; Tepper et al, 2018).

Corticostriatal inputs to SPNs and FSIs reconstructed in 3D using Imaris

The strength of synaptic connectivity from M1 and S1 to striatal SPNs and FSIs may derive from differences in the quantity and distribution of synaptic inputs. Based on our previous work (Lee et al. 2019), we hypothesized that SPNs have significantly more synaptic inputs from M1 compared to S1, but FSIs have a similar number of synaptic inputs from M1 and S1. To test for this, we quantified M1 and S1 inputs onto SPNs and FSIs from confocal 3D reconstructions using Imaris, similar to previous methods (Fogarty et al, 2013; Kuljis et al, 2019).

In brain slices from mice with M1 and S1 already labeled with sm.FPs, we patched and filled striatal neurons with biocytin for anatomical analysis. Raw fluorescence from single cell filled SPNs and FSIs was first converted into 3D "surface" objects using the surface tool in Imaris.

bioRxiv preprint doi: https://doi.org/10.1101/2023.03.06.531405; this version posted March 7, 2023. The copyright holder for this preprint (which was not certified by peer review) is the author/funder, who has granted bioRxiv a license to display the preprint in perpetuity. It is made available under aCC-BY-NC 4.0 International license.

Then, we constructed our neurons as "filament" objects because this enabled us to segment the dendritic spines, branch points, terminals, and reduce the inclusion of background fluorescence in the reconstruction (Fig. 2A).

The dual labeling of M1 and S1 permitted visualization of both cortical inputs simultaneously, but the distance between the pre and postsynaptic membrane is beyond the limitations of confocal light microscopy (Maidorn et al, 2016). To verify that sm.FPs from M1 and S1 represent putative synaptic inputs, we captured fluorescence from M1 and S1 axons along with a marker for the presynaptic scaffolding protein, bassoon, in a subset of patched neurons. Puncta from sm.FPs that labeled M1 and S1, colocalized with bassoon along the dendrites and spines of filled neurons for both SPNs and FSIs (Fig. 2B,C). However, the small size of presynaptic puncta (<0.5µm), combined with the large depth of our Z-stack (>50µm), limited our ability to capture inputs colocalized with bassoon in deeper parts of the Z-stack because of significant photobleaching of bassoon.

Therefore, to reconstruct M1 and S1 inputs onto striatal neurons, raw fluorescence from corticostriatal puncta was first masked onto the surface of the reconstructed neuron and then converted into 3D "spot" objects. We quantified the number and distribution of spots whose edge was within ≤0.5µm from the edge of the filament construction and identified them as putative presynaptic inputs (Fig 3A). To ensure that our counts were not limited to one side of the Z-stack or confounded by limited light penetration, the Z positions of the first and last appearance of a dendrite, the soma, as well as the Z positions of identified M1 and S1 inputs were obtained throughout the stack. We confirmed that there were no inputs counted outside the range of the neuron within the Z-stack and that M1 and S1 fluorescence penetrated equally throughout the stack for both cell types (Fig. 3-1a).

bioRxiv preprint doi: https://doi.org/10.1101/2023.03.06.531405; this version posted March 7, 2023. The copyright holder for this preprint (which was not certified by peer review) is the author/funder, who has granted bioRxiv a license to display the preprint in perpetuity. It is made available under aCC-BY-NC 4.0 International license.

386

387 **Preferential anatomical innervation of SPNs by M1 compared to S1 corticostriatal inputs**

388 On average, the total number of combined M1 and S1 inputs onto SPNs was greater than
389 FSIs but not significantly different (SPN = 418.55 +/- 52.97, N = 9 vs FSI = 306.2 +/- 78.11, N =
390 5, P = 0.2797, t = 1.132, df = 12, unpaired two tailed t-test), suggesting that we counted a similar
391 number of inputs within a given Z-stack for both cell types (Fig. 3-1b). However, there were
392 significantly more M1 than S1 inputs onto SPNs (SPN_{M1} = 244.44 +/- 29.10 vs SPN_{S1} = 174.111
393 +/- 32.53, N = 9, p = 0.0025, t = 4.339, df = 8, paired two tailed t-test) (Fig. 3-1c), resulting in a
394 considerably larger proportion of M1 than S1 inputs to SPNs (SPN_{M1} = 58.89 +/- 1.61% vs SPN_{S1}
395 = 41.11 +/- 1.61%, N = 9, p = 0.0008, t = 5.222, df = 8, paired two tailed t-test) (Fig. 3B). The
396 ratio of M1 inputs to S1 inputs on SPNs was significantly greater than a value of 1, indicating a
397 stronger preference for the M1 input ($SPN_{M1/S1}$ = 1.467 +/- 0.102, N = 9, p = 0.0025, t = 4.338, df
398 = 8, one sample t-test) (Fig. 3-1d).

399 In comparison, there were no substantial difference between the number and proportion of
400 M1 and S1 inputs onto FSIs (FSI_{M1} = 153.6 +/- 42.17 vs FSI_{S1} = 152.6 +/- 35.39, N = 5, p = 0.9849,
401 t = 0.02018, df = 4, paired two tailed t-test) (FSI_{M1} = 54.19 +/- 10.25% vs FSI_{S1} = 45.81 +/- 10.25%
402 , N = 5, p = 0.7332, t= 0.3656, df = 4, paired two tailed t-test) (Fig. 3B, 3-1c). Similarly, the ratio
403 of M1 to S1 inputs was not significantly different from a value of 1, suggesting no overall bias for
404 M1 or S1 ($FSI_{M1/S1}$ = 2.013 +/- 0.766, N = 5, p = 0.302, t = 1.183, df = 4, one sample t-test) (Fig.
405 3-1d).

406 Neither the cell type (F (1,12) = 1.282, p = 0.2797, two-way repeated measures ANOVA)
407 nor the origin of the cortical input (F (1,12) = 2.884, p = 0.1152, two-way repeated measures
408 ANOVA) had a significant effect on the variability of the number of inputs counted from M1 or

bioRxiv preprint doi: https://doi.org/10.1101/2023.03.06.531405; this version posted March 7, 2023. The copyright holder for this preprint (which was not certified by peer review) is the author/funder, who has granted bioRxiv a license to display the preprint in perpetuity. It is made available under aCC-BY-NC 4.0 International license.

S1. In addition, there was no significant interaction between the effects of cortical input and cell type on the number of inputs counted ($F(1,12) = 2.725$, $p = 0.1247$, two-way repeated measures ANOVA). However, a significant source of variability on counts stemmed from individual subject variability ($F(12,12) = 5.582$, $p = 0.0028$, two-way repeated measures ANOVA) (Fig 3C). M1 and S1 projection fields can vary along the mediolateral axis of the striatum, however we found no significant correlation between the ratio of M1 to S1 inputs and the mediolateral position of recorded neurons within the DLS (Fig 3-1e), leaving the source of individual variability unknown.

Altogether, although M1 and S1 inputs dually innervate SPNs and FSIs, M1 provides a greater number of synaptic inputs than S1 to SPNs, whereas M1 and S1 provide overall equal input to FSIs. These results complement previous measures of the functional synaptic strength of these inputs (Lee et al, 2019).

M1 and S1 inputs are similarly distributed in the proximal, medial, and distal regions of SPNs and FSIs

The spatial organization of synaptic inputs along the dendritic tree, in addition to the total number of inputs, is an important factor that can influence synaptic integration. To test if there are differences in the spatial distribution of M1 and S1 inputs to SPNs and FSIs, inputs were segmented based on their distance along the dendrites relative to the soma into 10µm bins. In both SPNs and FSIs, the distribution of M1 and S1 inputs closely followed each other and were found in proximal ($0 < 30$µm), medial ($30 < 100$µm), and distal regions (>100µm) of the neuron. Interestingly, the largest concentration of inputs was found near the soma for both SPNs and FSIs ($SPN_{M1\ 0\text{-}10\mu m} = 10.50 \pm 2.453\%$, $SPN_{S1\ 0\text{-}10\mu m} = 9.433 \pm 2.181\%$ N = 9; $FSI_{M1\ 0\text{-}10\mu m} = 14.31 \pm 4.473\%$, $FSI_{S1\ 0\text{-}10\mu m} = 10.88 \pm 2.981\%$, N = 5) (Fig. 3C). This was followed by a sharp dip in the

bioRxiv preprint doi: https://doi.org/10.1101/2023.03.06.531405; this version posted March 7, 2023. The copyright holder for this preprint (which was not certified by peer review) is the author/funder, who has granted bioRxiv a license to display the preprint in perpetuity. It is made available under aCC-BY-NC 4.0 International license.

number of inputs synapsing 20-30µm away from the soma of the SPNs, but this was not as prominent in FSIs. The number of M1 and S1 inputs peaked again at distances 70-80µm from the soma in SPNs but not in FSIs, and then decreased to near zero values at distal dendritic locations >100µm from the soma in both cell types (Fig. 3C).

Overall, M1 and S1 inputs were distributed similarly with no significant differences in the mean distance of M1 and S1 inputs from the soma in both SPNs and FSIs ($SPN_{M1\text{-}Soma}$ = 76.38 +/- 9.586µm vs $SPN_{S1\text{-}Soma}$ = 82.36 +/- 8.527µm, N = 9 , p = 0.2031, Wilcoxon matched pairs signed rank test; $FSI_{M1\text{-}Soma}$ = 59.44 +/- 7.555µm vs $FSI_{S1\text{-}Soma}$ = 65.97 +/- 6.427µm, N = 5, p = 0.2682, paired two tailed t-test) (Fig. 3-1f).

M1 and S1 inputs cluster onto SPNs but not FSIs

Since individual striatal neurons receive both M1 and S1 inputs, we wanted to know whether these inputs are localized near each other. To determine if M1 and S1 inputs form synaptic clusters, we measured the distance between inputs of the same type (M1-M1 or S1-S1) or inputs of different types (M1-S1). In SPNs, M1 inputs were found in proximity (~5µm) to other M1 inputs, and S1 inputs were also near other S1 inputs ($SPN_{M1\text{-}M1}$ = 4.390 +/- 0.5693µm vs $SPN_{S1\text{-}S1}$ = 4.532 +/- 0.4742µm, N = 9, p = 0.6728, t = 0.4383, df = 8, paired two tailed t-test). In FSIs, the shortest distance between M1-M1 inputs or S1-S1 inputs was similar to each other, but slightly larger than SPNs ($FSI_{M1\text{-}M1}$ = 6.680 +/- 1.220µm vs $FSI_{S1\text{-}S1}$ = 7.794 +/- 1.692µm, N = 5, p = 0.5832, t = 0.5961, df = 4 paired two tailed t-test) (Fig. 4A-C).

The cell type had a statistically significant effect on the variability of the distance between inputs from the same cortical region (F (1,12) = 6.768, p = 0.0232, two-way repeated measures

bioRxiv preprint doi: https://doi.org/10.1101/2023.03.06.531405; this version posted March 7, 2023. The copyright holder for this preprint (which was not certified by peer review) is the author/funder, who has granted bioRxiv a license to display the preprint in perpetuity. It is made available under aCC-BY-NC 4.0 International license.

ANOVA). Therefore, we compared between cell types and found that S1 inputs in SPNs were significantly closer together than in FSIs ($SPN_{S1\text{-}S1}$ = 4.532 +/- 0.4742 µm, N = 9 vs $FSI_{S1\text{-}S1}$ = 7.794 +/- 1.692µm, N = 5, p = 0.0358, t = 2.364, df = 12 unpaired two tailed t-test) (Fig. 4B). A similar trend was observed for M1 inputs but was not significant ($SPN_{M1\text{-}M1}$ = 4.390 +/- 0.5693µm, N = 9 vs $FSI_{M1\text{-}M1}$ = 6.680 +/- 1.220µm, N = 5, p =0.0747, t = 1.592, df = 12 unpaired two tailed t-test) (Fig 4B). These results indicate that inputs from the same cortical region tend to cluster more on SPN dendrites compared to FSI dendrites.

We next asked whether inputs from different cortical regions were more clustered in SPNs than FSIs. We found that the mean distance between an M1 and S1 input was significantly smaller in SPNs than in FSIs ($SPN_{S1\text{-}M1}$ = 4.727 +/- 0.6643µm, N = 9 vs $FSI_{S1\text{-}M1}$ = 8.609 +/- 1.023µm, N = 5, p = 0.0061, t = 3.321, df = 12, unpaired two- tailed t-test; $SPN_{M1\text{-}S1}$ = 7.156 +/- 1.565µm, N = 9 vs $FSI_{M1\text{-}S1}$ = 8.605 +/- 1.906µm, N = 5, p = 0.6309, Mann-Whitney U = 18.50) (Fig. 4D). There was a greater chance of S1 inputs being found within 5 µm of an M1 input in SPNs ($SPN_{S1\text{-}5\mu m}$ = 73.92 +/- 5.86%, p = 0.0049, t = 3.847, df = 8, $SPN_{M1\text{-}5\mu m}$ = 59.44 +/- 6.23%, p = 0.1912, t = 1.428, df = 8, N = 9, one sample t-test) (Fig. 4E). This was not the case for FSIs, as less than 50% of the S1 input colocalized within 5 µm of an M1 input ($FSI_{M1\text{-}5\mu m}$ = 51.18 +/- 15.33 %, p = 0.9483, t = 0.0689, df = 4, $FSI_{S1\text{-}5\mu m}$ = 39.86 +/- 6.71%, p = 0.2478, t = 1.352, df = 4, N = 5, one sample t-test) (Fig. 4E). These results indicate that the majority of S1 inputs onto SPNs form synaptic clusters with M1, and that clustering is more prominent in SPNs compared to FSIs.

These results led us to examine the spatial distribution of M1 and S1 inputs that form clusters within 5µm of each other. We observed that clustered M1-S1 inputs were distributed across the proximal, medial, and distal regions for both cell types and there was no differences in the mean distance from the soma for inputs that were part of a cluster ($SPN_{M1\text{-}S1}$ = 77.04 +/-

bioRxiv preprint doi: https://doi.org/10.1101/2023.03.06.531405; this version posted March 7, 2023. The copyright holder for this preprint (which was not certified by peer review) is the author/funder, who has granted bioRxiv a license to display the preprint in perpetuity. It is made available under aCC-BY-NC 4.0 International license.

9.943µm, $SPN_{S1\text{-}M1}$ = 78.76 +/- 8.807µm, N = 9; $FSI_{M1\text{-}S1}$ = 52.11 +/- 10.37µm, $FSI_{S1\text{-}M1}$ = 54.37 +/- 11.15µm, N = 5) (Fig. 4F). Similar to the distribution of individual M1 and S1 inputs, the highest concentration of clustered inputs was found 0-10µm from the soma ($SPN_{M1\ 0\text{-}10µm}$ = 12.71 +/- 3.572, $SPN_{S1\ 0\text{-}10µm}$ = 10.99 +/- 2.747, N = 9; $FSI_{M1\ 0\text{-}10µm}$ = 22.51 +/- 7.452%, $FSI_{S1\ 0\text{-}10µm}$ = 21.32 +/- 7.298%, N = 5) (Fig. 4G), with a second peak 60-70µm from the soma. The second peak was less prominent in FSIs compared to SPNs. Altogether, our results indicate that clustered M1 and S1 inputs are distributed across all regions of SPNs and FSIs but are located less densely at distal dendrites.

Discussion:

In this study, using dual fluorescent tracing, we measured the extent of corticostriatal projections from M1 and S1 to individual neurons in the DLS and identified cell-specific differences in the quantity and distribution of M1 and S1 inputs onto SPNs and FSIs. Our findings indicate that SPNs receive significantly more inputs from M1 compared to S1, while FSIs show no overall bias in the number of M1 or S1 inputs (Fig. 3). In addition, we found that M1 and S1 inputs have similar distributions across proximal, medial, and distal regions of SPNs and FSIs, but in SPNs, they are found near each other, forming synaptic clusters (Fig. 4). These results have implications for how M1 and S1 corticostriatal inputs modulate striatal circuitry and behavior.

Cell-specific differences in the number of inputs from M1 and S1 suggest stronger S1 connectivity to FSIs in the DLS

The convergence of M1 and S1 inputs to the DLS reflects its important role in sensorimotor integration (Makino et al, 2016; Gritton et al, 2019; Lipton et al, 2019; Matiros et al 2019). We observed extensive overlap of M1 and S1 projections onto individual neurons in the DLS, in

bioRxiv preprint doi: https://doi.org/10.1101/2023.03.06.531405; this version posted March 7, 2023. The copyright holder for this preprint (which was not certified by peer review) is the author/funder, who has granted bioRxiv a license to display the preprint in perpetuity. It is made available under aCC-BY-NC 4.0 International license.

agreement with previous experiments (Fig. 1B, Fig. 2B, C) (Hoffer & Alloway, 2001; Hunnicutt et al, 2016; Hooks et al, 2018).

Due to our use of biocytin to label patched neurons, we did not use genetic labels for D1 and D2 SPNs, or parvalbumin for FSIs. However, in our study the proportion of inputs from M1 and S1 to SPNs had low variability (Fig 3C), suggesting that D1 and D2 SPNs have a similar distribution of M1 and S1 inputs, which we previously demonstrated through optogenetic stimulation of M1 and S1 inputs (Lee et al, 2019). The more notable differences in M1 and S1 innervation were found between SPNs and FSIs, and we distinguished patched FSIs from SPNs by their larger soma size, varicose aspiny dendrites, and high frequency spiking compared to SPNs, which has been reported in previous studies (Fig 1C-F, Fig. 1-1) (Kawaguchi, 1993 & 1997; Tepper et al, 2018). While most parvalbumin interneurons in the striatum are FSIs, there are likely regional subtypes of FSIs with distinct responses and connectivity to cortical brain regions (Monteiro et al, 2018; Tokarska & Silberberg, 2022). Future experiments could use further genetic cell typing, which could help clarify the variability we observed between individual cells.

SPNs and FSIs require many excitatory inputs to generate action potentials due to their hyperpolarized resting membrane voltages seen in Fig. 1-1e (Kawaguchi, 1993 & 1997; Tepper et al, 2018). A greater quantity of inputs leads to increased EPSPs because inputs can spatially summate on dendrites (Magee, 2000). M1 and S1 can form synaptic contacts onto the same SPN or FSI (Fig. 2B) (Ramanathan et al, 2002; Johansson & Silberberg, 2020; Charpier et al, 2020), but DLS SPNs have weak responses to sensory stimuli and strong responses to motor activity (Lee et al, 2019; Matiros et al, 2018, Charpier et al, 2020). In contrast, FSIs respond to M1 and S1 stimulation with EPSPs of similar amplitude (Lee et al, 2019; Johansson & Silberberg, 2020). Directly comparing the number of inputs from M1 or S1 revealed no significant differences

bioRxiv preprint doi: https://doi.org/10.1101/2023.03.06.531405; this version posted March 7, 2023. The copyright holder for this preprint (which was not certified by peer review) is the author/funder, who has granted bioRxiv a license to display the preprint in perpetuity. It is made available under aCC-BY-NC 4.0 International license.

between SPNs and FSIs, however we found that SPNs had significantly fewer inputs from S1 compared to M1, and that number of inputs between M1 and S1 was similar in FSIs (Fig 3-1c). The reduced innervation by S1 compared to M1 in SPNs, but equal innervation compared to M1 in FSIs suggest that S1 promotes the feedforward inhibition of SPNs by preferentially activating FSIs over SPNs (Lee et al 2019, Johansson and Silberberg 2020).

A large source of variability in the counts stemmed from our group of FSIs (Fig 3-1c, see Anova results). However, this is not due to differences in the penetration of light from our sm.FP constructs during imaging (Fig. 3-1a), or the total number of inputs counted between SPNs and FSIs (Fig. 3-1b). Moreover, despite a denser overlap of M1 and S1 in the more lateral aspects of the striatum we found no major correlation between lateral position and the ratio of M1/S1 inputs. This might indicate that ratio of M1 to S1 inputs to SPN and FSIs is consistent across the DLS (Fig. 1G, Fig. 3-1e) instead of the possibility that the mediolateral position of a patched neuron biased innervation patterns towards M1 or S1.

The location of M1 and S1 inputs onto SPNs and FSIs suggest integration through spatiotemporal mechanisms

The anatomical measures indicate that the quantity of synapses partly account for differences between cell types. The distance between the input from the soma is also important because distal inputs undergo electrotonic decay and result in smaller EPSPs recorded at the soma when compared to proximal inputs (Rall, 1967; Magee, 2000; Straub et al, 2016). We found that M1 and S1 inputs had similar distributions across regions of the neuron for both SPNs and FSIs. A large proportion of apparent inputs were observed closer to the soma for SPNs (Fig. 3C). However, reports using correlative light and electron microscopy (CLEM) with VGLUT1, a

bioRxiv preprint doi: https://doi.org/10.1101/2023.03.06.531405; this version posted March 7, 2023. The copyright holder for this preprint (which was not certified by peer review) is the author/funder, who has granted bioRxiv a license to display the preprint in perpetuity. It is made available under aCC-BY-NC 4.0 International license.

547 synaptic marker expressed in corticostriatal terminals, have also observed cortical terminals near
548 the cell body but demonstrated that true asymmetric synapses form at the dendritic spines of SPNs,
549 with few inputs to the dendritic shafts and cell body (Reiner et al, 2010; Lei et al, 2013, Deng et
550 al, 2015).

551 In SPNs, spines are prominent on the primary dendrites distal to the first dendritic
552 ramifications (Fig. 1C, 2A) (Wilson & Groves,1980), likely explaining why we observed a drop
553 in counts in more proximal regions (Fig. 3C). Interestingly, the number of M1 and S1 inputs
554 peaked again at medial dendritic distances (70-80µm) (Fig. 3C), where SPNs have active calcium
555 conductances that contribute to the generation of "up-states" and increased excitability (Plotkin et
556 al, 2011). Other reports have shown stronger synaptic responses in SPNs and the presence of
557 synaptic clusters at similar dendritic locations (Straub et al, 2016; Hwang et al, 2022). In contrast,
558 "up-states" have not been demonstrated in FSIs, suggesting that they integrate inputs passively
559 (Plenz and Kitai, 1998); Our data is consistent with reports that corticostriatal synapses are broadly
560 distributed onto the dendrites of FSIs (Ramanathan et al, 2002; Nakano et al, 2018; Zheng et al,
561 2021).

562 SPNs can perform sublinear, linear, and supralinear integration of excitatory inputs
563 depending on the timing and location of the input (Carter et al, 2007, Straub et al, 2016). The
564 clustering of synapses is optimized for long-term plasticity because the coincident activation of
565 multiple synapses in spines that are in close together on a dendrite can produce a self-regenerating
566 dendritic spike, which is stronger and longer lasting than an EPSP. (Losonczy & Magee, 2006;
567 Carter et al, 2007; Kastellakis & Poirazi, 2019, Du et al, 2017). Although we observed less S1
568 inputs compared to M1 in SPNs (Fig. 3A, B), the majority (> 50%) of S1 inputs were in proximity
569 (< 5µm) to a neighboring S1 input or M1 input, and this was not the case for FSIs (Fig. 4A-D).

bioRxiv preprint doi: https://doi.org/10.1101/2023.03.06.531405; this version posted March 7, 2023. The copyright holder for this preprint (which was not certified by peer review) is the author/funder, who has granted bioRxiv a license to display the preprint in perpetuity. It is made available under aCC-BY-NC 4.0 International license.

These results support the theory that SPNs can act as coincidence detectors for M1 and S1 and integrate signals from these cortical regions through temporal and spatial summation by clustering sensorimotor inputs. Critically, it has been observed that stimulation of M1 inputs induces an initial membrane depolarization in SPNs that is quickly enhanced by activity generated from S1 (Charpier et al, 2020), and M1 inputs from mice trained on motor tasks form active clusters on the spines of SPNs in the DLS (Hwang et al, 2022).

Implications of findings on sensorimotor integration by SPNs and FSIs in the DLS

In vivo, during sensorimotor learning, SPNs form ensembles that are highly active during the initiation and termination of task-related movements associated with reward (Matiros et al, 2018; Gritton et al, 2019). PV-FSIs have an important contribution to SPN ensemble formation in the DLS (Matiros et al, 2018; Gritton et al, 2019). The cell specific distribution of M1 and S1 to the DLS that is seen in our results likely contributes to organizing which cells are active during this process.

Synaptic clustering greatly increases the likelihood that activity from M1 and S1 is coincidentally detected on short sections of the dendritic membrane, leading to large depolarizations and changes in plasticity (Carter al al, 2007; Kastellakis & Poirazi, 2019). This increases the chance that these inputs become associated with other cortical and thalamic regions when there is convergent activity (Carter et al, 2007; Huerta-Ocampo et al, 2014, Makino et al, 2016). Therefore, it is likely that while S1 alone does not evoke strong responses in SPNs, SPNs that receive convergent activity from task related M1 and S1 neurons will overcome local inhibition by FSIs and increase the probability of firing an action potential. As a result, they

bioRxiv preprint doi: https://doi.org/10.1101/2023.03.06.531405; this version posted March 7, 2023. The copyright holder for this preprint (which was not certified by peer review) is the author/funder, who has granted bioRxiv a license to display the preprint in perpetuity. It is made available under aCC-BY-NC 4.0 International license.

become part of task related circuits in the DLS that underlie habitual responses to sensory stimuli (Matiros et al, 2018; Lipton et al, 2019).

In conclusion, the organization of M1 and S1 inputs to the DLS suggest that activity from S1 will preferentially excite the striatal FSI population, leading to feed forward inhibition of SPNs during sensorimotor integration. Our findings have significant implications for how corticostriatal circuits encode learned movements. Future investigations should examine if there are cell-specific requirements for plasticity in corticostriatal inputs to SPNs and FSIs.

bioRxiv preprint doi: https://doi.org/10.1101/2023.03.06.531405; this version posted March 7, 2023. The copyright holder for this preprint (which was not certified by peer review) is the author/funder, who has granted bioRxiv a license to display the preprint in perpetuity. It is made available under aCC-BY-NC 4.0 International license.

Figure Legends:

Figure 1. Viral circuit mapping of M1 and S1 corticostriatal projections to dorsal striatal SPNs and FSIs. (A) Viral circuit mapping strategy highlighting spaghetti monster injections into M1 and S1 from a top-down view (left) and the corticostriatal projection pattern onto biocytin filled striatal cells from a sagittal view (right). **(B)** *Top-left*: Low magnification view of a coronal striatal section containing the M1 sm.FP injection site and corticostriatal projections to the dorsolateral striatum. *CC* = corpus callosum, *DLS* = dorsolateral striatum. *Top-Right*: Low magnification view of a coronal striatal section with S1 corticostriatal projections labeled with sm.FPs. *Bottom-Left*: Low magnification view of merged fluorescence from S1 and M1 corticostriatal projections innervating a striatal SPN filled with biocytin (white box). *Bottom-Right*: High magnification inset bottom-left image with corticostriatal innervation by M1 and S1 onto a biocytin filled SPN. **(C)** *Left:* Pseudo colored representative image of a biocytin filled SPN with spiny dendrites (inset). *Right:* Pseudo colored representative image of a biocytin filled FSI with aspiny dendrites (inset). **(D)** *Left:* Average number of primary dendrites (note that FSIs have more primary dendrites extending from the soma compared to SPNs). *Right:* Average cross-sectional diameter of the soma **(E)** Comparison of mean instantaneous firing frequency and mean half-height width at steady state permits differentiation of FSIs from SPNs due to their fast firing rates. **(F)** *Left:* Average max firing frequency. *Right:* Average interspike interval. **(G)** Schematic representation of the recording location of the SPNs and FSIs in our dataset (note that all cells were recorded in the anterior dorsal striatum where M1 and S1 innervation was dense).

Figure 1-1. Morphological and electrophysiological properties of SPNs and FSIs. (a) Mean cross sectional diameter of the dendritic field. **(b)** Mean depth of the dendritic field along the z-

bioRxiv preprint doi: https://doi.org/10.1101/2023.03.06.531405; this version posted March 7, 2023. The copyright holder for this preprint (which was not certified by peer review) is the author/funder, who has granted bioRxiv a license to display the preprint in perpetuity. It is made available under aCC-BY-NC 4.0 International license.

642 axis. **(c)** Mean half height width (HWH) amplitude. **(d)** Mean instantaneous firing frequency. **(e)**
643 Mean resting membrane potential voltage. **(f)** Mean input resistance.
644
645 **Figure 2. 3D reconstructions of striatal neurons and confirmation of S1 and M1 synaptic**
646 **puncta. (A)** 3D-reconstruction of biocytin filled SPNs and FSIs into a "surface" and "filament"
647 object in Imaris. **(B)** Representative raw fluorescence from biocytin, the presynaptic protein
648 bassoon, M1, and S. **(C)** Merged image from **B** demonstrating S1 and M1 presynaptic inputs dually
649 innervating an SPN (top) and FSI (bottom).
650
651 **Figure 3. Differential innervation by S1 and M1 to SPNs and FSIs.** (**A)** Magnified view of raw
652 fluorescence (left) from S1 and M1 corticostriatal projections onto a biocytin filled SPN (top) and
653 FSI (bottom) with their associated 3D-reconstructions (right). **(B)** Average percent innervation by
654 M1 and S1. **(C**) Mean distribution of S1 and M1 inputs across the neuron when measuring the
655 distance from the soma along the length of a dendrite.
656
657 **Figure 3-1**. **Distribution properties of S1 and M1 inputs to SPNs and FSIs. (A**) Z-positions of
658 the first and last appearance of a dendrite, and the soma of reconstructed SPNs (Left) and FSIs
659 (Right) compared with the Z positions of their associated S1 and M1 inputs **(B)** Mean total number
660 of combined S1 and M1 spots counted within 0.5µm of the filament constructed SPN or FSI **(C)**
661 Mean number of spots counted from S1 and M1 within 0.5µm of the filament edge **(D)** Mean ratio
662 of M1 spots to S1 spots counted within 0.5µm of the filament edge **(E)** Comparison of M1/S1
663 ratio with the mediolateral position of the neuron it was recorded from; black dots = SPNs (n=8),

bioRxiv preprint doi: https://doi.org/10.1101/2023.03.06.531405; this version posted March 7, 2023. The copyright holder for this preprint (which was not certified by peer review) is the author/funder, who has granted bioRxiv a license to display the preprint in perpetuity. It is made available under aCC-BY-NC 4.0 International license.

664 gray dots = FSIs (n=4). **(F)** Mean distance of an S1 and M1 input from the soma when measured
665 along the length of the dendrite.

666 **Figure 4. S1 and M1 input cluster on SPNs but not in FSIs. (A)** Representative image of
667 fluorescence from M1 (red) and S1 (green) masked onto the dendrites of an SPN (Left) and an FSI
668 (Right). **(B)** Mean distance between the nearest input from the same cortical region. **(C)** Mean
669 distribution of the shortest distance to the nearest input from the same cortical region. **(D)** Mean
670 distance between inputs from different cortical regions. **(E)** Mean percent of S1 and M1 Inputs
671 that colocalized with an increasing distance threshold for SPNs (Right) and FSIs (Left). **(F)** Mean
672 distance from the soma when measured along the length of the dendrite for S1 and M1 spots that
673 colocalized within 5μm of each other. **(G)** Distribution of colocalized spots from **F**.

674

675

	ML	AP	DV
SPN, *n* = 8	1.738 +/- 0.06mm	1.12 +/- 0.04mm	-2.265 +/- 0.10mm
FSI, *n* = 4	1.70 +/- 0.19mm	1.04 +/- 0.11mm	-2.125 +/- 0.10mm.

676

677 **Table 1. Position of recorded striatal neurons from ex-vivo slices relative to bregma.** The
678 medial lateral (ML), anterior posterior (AP), and dorsal ventral (DV) position of the recorded
679 neuron within the striatum relative to bregma.

680

bioRxiv preprint doi: https://doi.org/10.1101/2023.03.06.531405; this version posted March 7, 2023. The copyright holder for this preprint (which was not certified by peer review) is the author/funder, who has granted bioRxiv a license to display the preprint in perpetuity. It is made available under aCC-BY-NC 4.0 International license.

References

Allen Reference Atlas – Mouse Brain [brain atlas]. Available from atlas.brain-map.org.

Bagreddine N, Zalcman G, Appaix F, Saudou F, Archard S (2022) Spatiotemporal reorganization of corticostriatal networks encodes motor movements. Cell Reports 39 (1): 110623

Blue Brain Project (2015) eFEL. Available online at: https://github.com/BlueBrain/eFEL

Bolam JP, Hanley JJ, Booth PAC, Bevan MD (2002) Synaptic Organization of the basal ganglia. Journal of Anatomy 196(4): 527-542.

Carter AG, Soler-Llavina GJ, Sabatini BL (2007) Timing and location of synaptic inputs determines modes of subthreshold integration in striatal medium spiny neurons. Journal of Neuroscience 27(33): 8967-8977.

Charpier S, Pidoux M, Mahon S (2020) Converging sensory and motor cortical inputs onto the same striatal neurons: An in-vivo intracellular investigation. PLOS ONE 15: e0228260.

Deng Y, Lanciego J, Kerkerian-Le Goff L, Coulon P, Salin P, Kachidian P, Lei W, Del Mar N, Reiner A (2015) Differential organization of cortical inputs to striatal projection neurons of the matrix compartment in rats. Frontiers in Systems Neuroscience 9 (51).

Du K, Yu-Wei W, Lindroos R, Liu Y, Rozsa B, Katona G, Ding JB, Kotaleski JH (2017) Cell-type-specific inhibition of dendritic plateau potential in striatal spiny projection neurons. PNAS Plus 114 (36) e7612-e7621.

Fino E, Glowinski J, Venance L (2005) Bidirectional activity-dependent plasticity at corticostriatal synapses. The Journal of Neuroscience 25(49); 11289-11287.

Fino E & Venance L (2011) Spike-timing dependent plasticity in striatal interneurons. Neuropharmacology 60(5): 780-788

bioRxiv preprint doi: https://doi.org/10.1101/2023.03.06.531405; this version posted March 7, 2023. The copyright holder for this preprint (which was not certified by peer review) is the author/funder, who has granted bioRxiv a license to display the preprint in perpetuity. It is made available under aCC-BY-NC 4.0 International license.

703 Fogarty MJ, Hammond LA, Kanjhan R, Bellingham MC, Noakes PG (2013) A method for the
704 three-dimensional reconstruction of Neurobiotin^{TM}-filled neurons and the location of their synaptic
705 inputs. Frontiers in Neural Circuits 7(153).
706 Gastinger M (2022) Python 3.7-Imaris-Xtensions. (https://github.com/Ironhorse1618/Python3.7-
707 Imaris-XTensions) , Github
708 Ghasemi A, Zahediasl S (2012). Normality Test for Statistical Analysis: A Guide for Non-
709 Statisticians. International Journal of Endocrinology and Metabolism 10(2): 486-489.
710 Gritton HJ, Howe WM, Romano MF, DiFeliciantonio AG, Kramer MA, Saligrama V, Bucklin
711 ME, Zemel D, Han X (2019) Unique contributions of parvalbumin and cholinergic interneurons
712 in organizing striatal networks during movement. Nature Neuroscience 22, 586-597.
713 Hintiryan H, Foster NN, Bowman I, Bay M, Song MY, Gou L, Yamashita S, Bienkowski MS,
714 Zingg B, Zhu M, Yang XW, Shih JC, Toga AW, Dong HW (2016) The mouse cortico-striatal
715 projectome. Nature Neuroscience 19, 1100-1114.
716 Hjorth JJJ, Kozlov A, Carannante I, Nylén JF, Lindroos R, Johansson Y, Tokarska A, Dorst MC,
717 Suryanarayana SM, Silberberg G, Kotaleski JH, Grillner S (2020) The Microcircuits of striatum
718 in silico. PNAS 117(17): 9554-9565.
719 Hoffer ZS & Alloway KD (2001) Organization of corticostriatal projections from the vibrissal
720 representations in the primary motor and somatosensory cortical areas of rodents. The Journal of
721 Comparative Neurology 439(1): 87-103.
722 Hooks BM, Papale AE, Paletzki RF, Feroze MW, Eastwood BS, Couey JJ, Winnubst J,
723 Chandrashekar J, Gerfen CR (2018) Topographic precision in sensory and motor corticostriatal
724 projections varies across cell type and cortical area. Nature Communications *9*, 3549.

bioRxiv preprint doi: https://doi.org/10.1101/2023.03.06.531405; this version posted March 7, 2023. The copyright holder for this preprint (which was not certified by peer review) is the author/funder, who has granted bioRxiv a license to display the preprint in perpetuity. It is made available under aCC-BY-NC 4.0 International license.

725 Huerta-Ocampo I, Mena-Segovia J, Bolam JP (2014) Convergence of cortical and thalamic input
726 to direct and indirect pathway medium spiny neurons in the striatum. Brain Structure and Function
727 219: 1787-1800.
728 Hunnicut BJ, Jongbloets BC, Birdsong WT, Gertz KJ, Zhong H, Mao T (2016) A comprehensive
729 excitatory input map of the striatum reveals novel functional organization. eLife 5: e19103.
730 Hwang FJ, Roth RH, Wu YW, Kwon DK, Liu Y, Ding JB (2022) Motor learning selectively
731 strengthens cortical and striatal synapses of motor engram neurons. Neuron 110(17): 2790-2081e5.
732 Johansson Y & Silberberg G (2020) The Functional Organization of Cortical and Thalamic Inputs
733 onto Five Types of Striatal Neurons is determined by Source and Target Cell Identities. Cell
734 Reports 30(4): 1178- 1194.
735 Kawaguchi Y (1993) Physiological, morphological, and histochemical characterization of three
736 classes of interneurons in rat neostriatum. Journal of Neuroscience 13(11), 4908-4923.

737 Kawaguchi Y (1997) Neostriatal cell subtypes and their functional roles. Neuroscience Research,
738 27(1): 1-8.

739 Kastellakis G & Poirazi P (2019) Synaptic Clustering and Memory Formation. Frontiers in
740 Molecular Neuroscience 12 (300): 1-13.
741 Klein C. (2022) Heka Patchmaster Importer.
742 (https://github.com/ChristianKeine/HEKA_Patchmaster_Importer), Github
743 Kreitzer AC, Malenka R (2008) Striatal plasticity and basal ganglia circuit function. Neuron
744 60(4):543-554.
745 Kuljis DA, Park E, Telmer CA, Lee J, Ackerman DS, Bruchez MP, Barth AL (2019) Fluorescence-
746 based Quantitative Synapse Analysis for Cell Type-Specific Connectomics. eNeuro 6(5)
747 ENEURO.0193-19.

bioRxiv preprint doi: https://doi.org/10.1101/2023.03.06.531405; this version posted March 7, 2023. The copyright holder for this preprint (which was not certified by peer review) is the author/funder, who has granted bioRxiv a license to display the preprint in perpetuity. It is made available under aCC-BY-NC 4.0 International license.

748 Lee CR, Yonk AJ, Wiskerke J, Paradiso KG, Tepper JM, Margolis DJ (2019) Opposing Influence
749 of Sensory and Motor Cortical Input on Striatal Circuitry and Choice Behavior. Current Biology
750 29:1313-1323 e1315.

751 Lei W, Deng Y, Liu B, Mu S, Guley MN, Wong T, Reiner A (2013) Confocal Laser Scanning
752 Microscopy and Ultrastructural Study of VGLUT2 Thalamic Input to Striatal Projection Neurons
753 in Rats. The Journal of Comparative Neurology 521: 1354-1377.

754 Lipton DM, Gonzales BJ, Citri A (2019) Dorsal Striatal Circuits for Habits, Compulsions and
755 Addictions. Frontiers in Systems Neuroscience 13(28):1-14.
756 Losonczy A, Magee JC (2006) Integrative Properties of Radial Oblique Dendrites in Hippocampal
757 CA1 Pyramidal Neurons. Neuron 50 (2): 291-307.

758 Machado S, Cunha M, Velasques B, Minc D, Teixeira S, Domingues CA, Silva JG, Bastos VH,
759 Budde H, Cagy M, Basile L, Piedade R, Ribeiro P (2010) Sensorimotor integration: basic concepts,
760 abnormalities related to movement disorders and sensorimotor training-induced cortical
761 reorganization. Rev. Neurol 1;57(7): 427-436.

762 Magee JC (2000) Dendritic integration of excitatory synaptic input. Nature Reviews Neuroscience
763 1, 181-190.

764 Makino H, Hwang EJ, Hedrick NG, Komiyama T (2016) Circuit Mechanisms of Sensorimotor
765 learning. Neuron 92(4): 705-721.
766 Maidorn M, Rizzoli SO, Opazo F (2016) Tools and limitations to study the molecular composition
767 of synapses by fluorescence microscopy. The Biochemical Journal 473(20): 3385-3399.

bioRxiv preprint doi: https://doi.org/10.1101/2023.03.06.531405; this version posted March 7, 2023. The copyright holder for this preprint (which was not certified by peer review) is the author/funder, who has granted bioRxiv a license to display the preprint in perpetuity. It is made available under aCC-BY-NC 4.0 International license.

768 Matiros N, Burgess AA, Graybiel AM (2018) Inversely Active Striatal Projections and
769 Interneurons Selectively Delimit Useful Behavioral Sequences. Current Biology 28(4): 560-
770 573.e5.
771 Mishra P, Pandey CM, Singh U, Gupta A, Sahu C, Keshri A (2019) Descriptive Statistics and
772 Normality Test for Statistical Data. Annals of Cardiac Anaesthesia 22(1): 67-72
773 Monteiro P, Barak B, Zhou Y, McRae R, Rodriguez D, Wickersham IR, Feng G (2018)
774 Dichotomous Parvalbumin Interneuron populations in dorsolateral and dorsomedial striatum.
775 Journal of Physiology 596(16): 3695-3707.
776 Nakano Y, Karube F, Hirai Y, Kobayashi K, Hioki H, Okamoto S, Kameda H, Fujiyama F (2018)
777 Parvalbumin-producing striatal interneurons receive excitatory inputs onto proximal dendrites
778 from the motor thalamus in male mice. Journal Of Neuroscience Research 97(7): 1186-1207.
779 Perrin E & Venance L (2019) Bridging the gap between striatal plasticity and learning. Current
780 Opinion in Neurobiology 54: 104-112.
781 Plenz D & Kitai ST (1998) Up and down states in striatal medium spiny neurons simultaneously
782 recorded with spontaneous activity in fast-spiking interneurons studied in cortex-striatum-
783 substantia nigra organotypic cultures. The Journal of Neuroscience 18, 266-283.
784 Plotkin JL, Day M, Surmeier DJ (2011) Synaptically driven state transitions in distal dendrites of
785 striatal spiny neurons. Nature Neuroscience 14, 881-888.
786 Rall W (1967) Distinguishing theoretical synaptic potentials computed for different soma-
787 dendritic distributions of synaptic input. Journal of neurophysiology 30:1138-1168.
788 Ramanathan S, Hanley JJ, Deniau JM, Bolam JP (2002) Synaptic Convergence of Motor and
789 Somatosensory Cortical Afferents onto GABAergic Interneurons in the rat striatum. The Journal
790 of Neuroscience 22(18): 8158-8169.

bioRxiv preprint doi: https://doi.org/10.1101/2023.03.06.531405; this version posted March 7, 2023. The copyright holder for this preprint (which was not certified by peer review) is the author/funder, who has granted bioRxiv a license to display the preprint in perpetuity. It is made available under aCC-BY-NC 4.0 International license.

Reiner A, Hart NM, Lei W, Deng Y (2010) Corticostriatal projection neurons - dichotomous types and dichotomous functions. Frontiers in Neuroanatomy 4 (142)

Smith JB, Chakrabarti S, Mowery TM, Alloway KD (2022) Convergence of forepaw somatosensory and motor cortical projections in the striatum, claustrum, thalamus, and pontine nuclei of cats. Brain Structure and Function 227(1): 361-379.

Stern EA, Jaeger D, Wilson CJ (1998) Membrane potential synchrony of simultaneously recorded striatal spiny neurons in vivo. Nature 394, 475-478.

Straub C, Saulnier JL, Bègue A, Feng DD, Huang KW, Sabatini BL (2016) Principles of synaptic organization of GABAergic interneurons in the striatum. Neuron 92(1): 84-92.

Tepper J, M, Koós T, Ibáñez-Sandoval O, Tecuapetla F, Faust TW, Assous M (2018) Heterogeneity and Diversity of Striatal GABAergic Interneurons: Update 2018. Frontiers in neuroanatomy 12, 91.

Tokarska A & Silberberg G (2022) GABAergic interneurons expressing the α2 nicotinic receptor subunit are functionally integrated in the striatal microcircuit. Cell Reports 39(8).

Van Geit W, Gevaert M, Chindemi G, Rössert C, Courcol JD, Muller EB, Schürmann F, Segev I, Markram H (2016) BluePyOpt: Leveraging Open Source Software and Cloud Infrastructure to Optimize Model Parameters in Neuroscience. Frontiers in Neuroinformatics 10(17)

Viswanathan S, Williams ME, Bloss EB, Stasevich TJ, Speer CM, Nern A, Pfeiffer BD, Hooks BM, Li WP, English BP, Tian T, Henry GL, Macklin JJ, Patel R, Gerfen CR, Zhuang X, Wang Y, Rubin GM, Looger LL (2015) High-performance probes for light and electron microscopy. Nature Methods 12(6), 568–576.

bioRxiv preprint doi: https://doi.org/10.1101/2023.03.06.531405; this version posted March 7, 2023. The copyright holder for this preprint (which was not certified by peer review) is the author/funder, who has granted bioRxiv a license to display the preprint in perpetuity. It is made available under aCC-BY-NC 4.0 International license.

812 Willett JA, Cao J, Dorris DM, Johnson AG, Ginnari LA, Meitzen J (2019) Electrophysiological
813 Properties of Medium Spiny Neuron Subtypes in the Caudate-Putamen of Prepubertal Male and
814 Female *Drd1a*-tdTomato Line 6 BAC Transgenic Mice. eNeuro *6*(2) ENEURO.0016-19.2019.

815 Wilson CJ, Groves PM (1980) Fine structure and synaptic connections of the common spiny
816 neuron of the rat neostriatum: A study employing the intracellular injection of horseradish
817 peroxidase. The Journal of Comparative Neurology 194 (3): 599-615.

818 Zheng X, Sun L, Bingbing L, Huang Z, Zhu Y, Chen T, Jia L, Li Y, Lei W (2021) Morphological
819 Study of the Cortical and Thalamic Glutamatergic Synaptic Inputs of Striatal Parvalbumin
820 Interneurons in Rats. Neurochemical Research 46: 1659-1673.
821 Zhu X, Huang L, Zheng Y, Gong W (2019) Ultrafast optical clearing method for three-dimensional
822 imaging with cellular resolution. PNAS 116(23): 11480-11489

bioRxiv preprint doi: https://doi.org/10.1101/2023.03.06.531405; this version posted March 7, 2023. The copyright holder for this preprint (which was not certified by peer review) is the author/funder, who has granted bioRxiv a license to display the preprint in perpetuity. It is made available under aCC-BY-NC 4.0 International license.

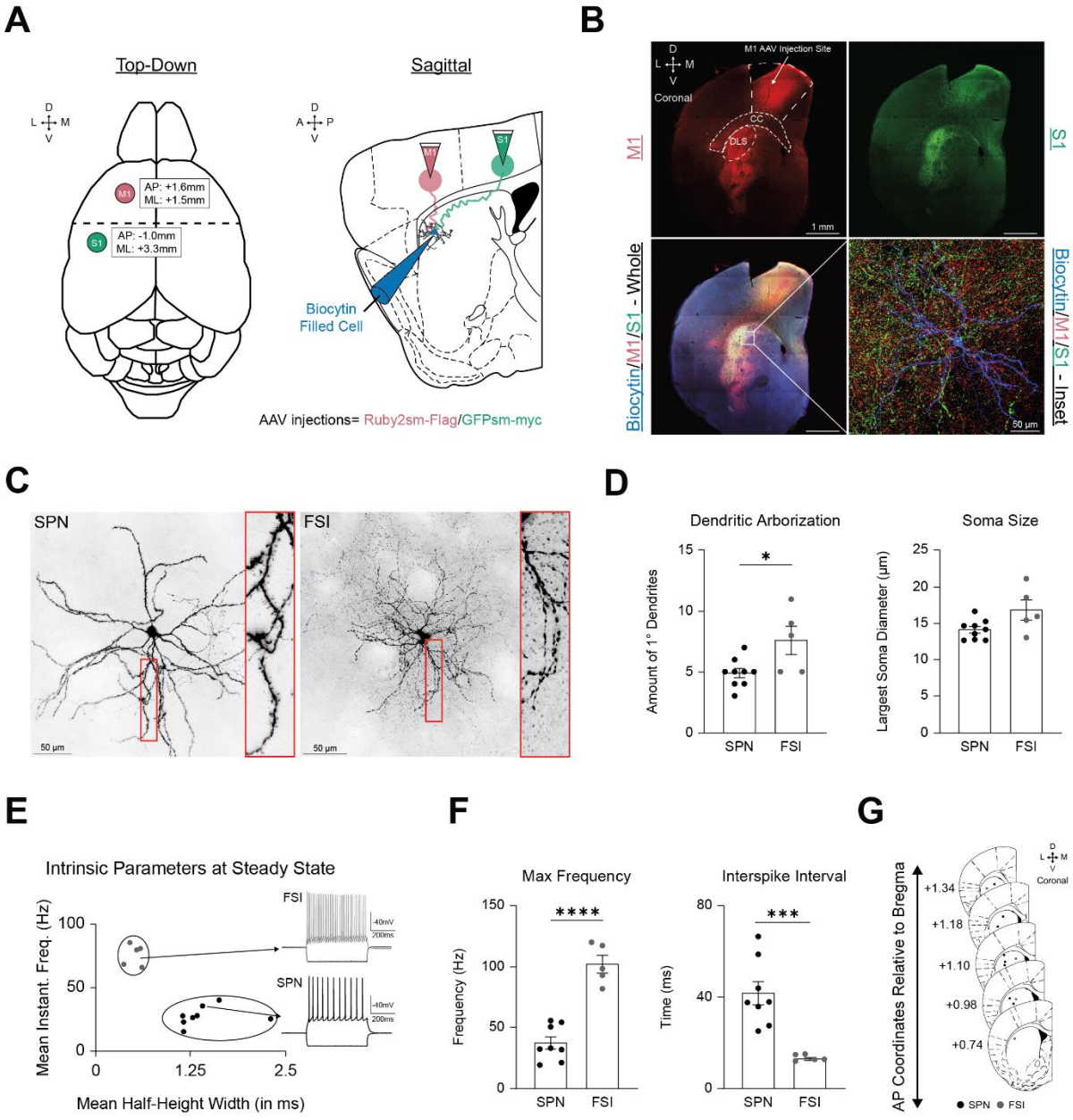

bioRxiv preprint doi: https://doi.org/10.1101/2023.03.06.531405; this version posted March 7, 2023. The copyright holder for this preprint (which was not certified by peer review) is the author/funder, who has granted bioRxiv a license to display the preprint in perpetuity. It is made available under aCC-BY-NC 4.0 International license.

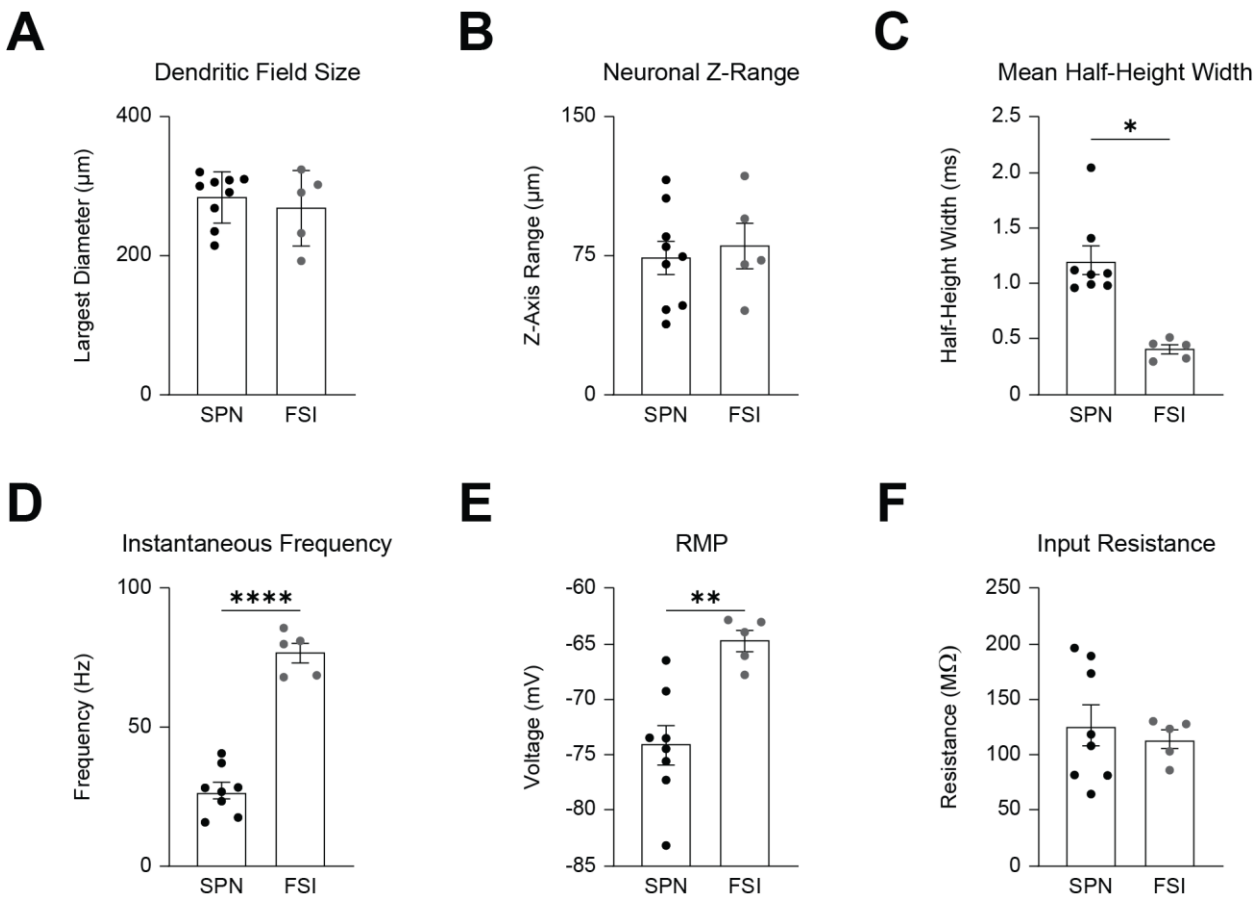

bioRxiv preprint doi: https://doi.org/10.1101/2023.03.06.531405; this version posted March 7, 2023. The copyright holder for this preprint (which was not certified by peer review) is the author/funder, who has granted bioRxiv a license to display the preprint in perpetuity. It is made available under aCC-BY-NC 4.0 International license.

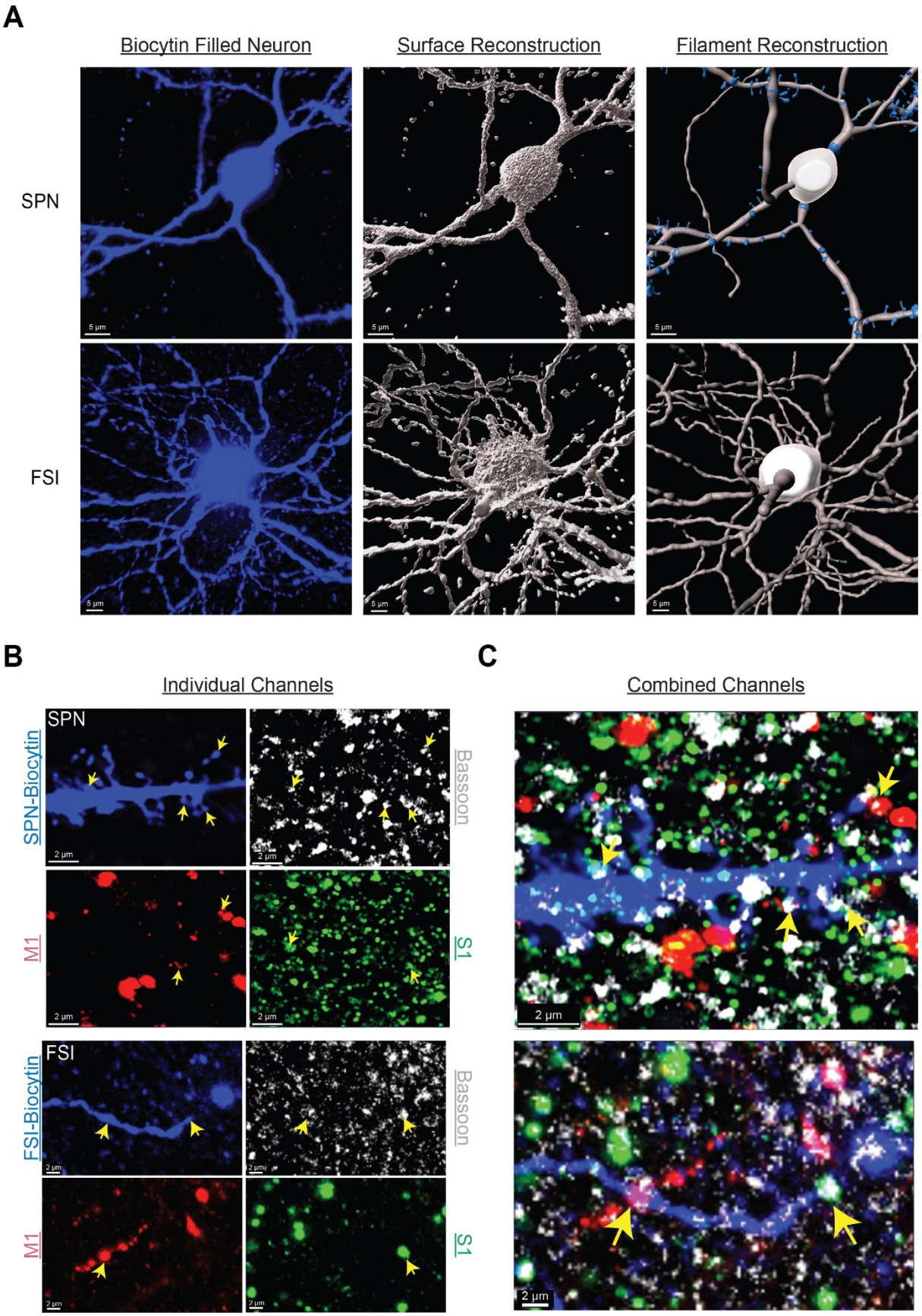

bioRxiv preprint doi: https://doi.org/10.1101/2023.03.06.531405; this version posted March 7, 2023. The copyright holder for this preprint (which was not certified by peer review) is the author/funder, who has granted bioRxiv a license to display the preprint in perpetuity. It is made available under aCC-BY-NC 4.0 International license.

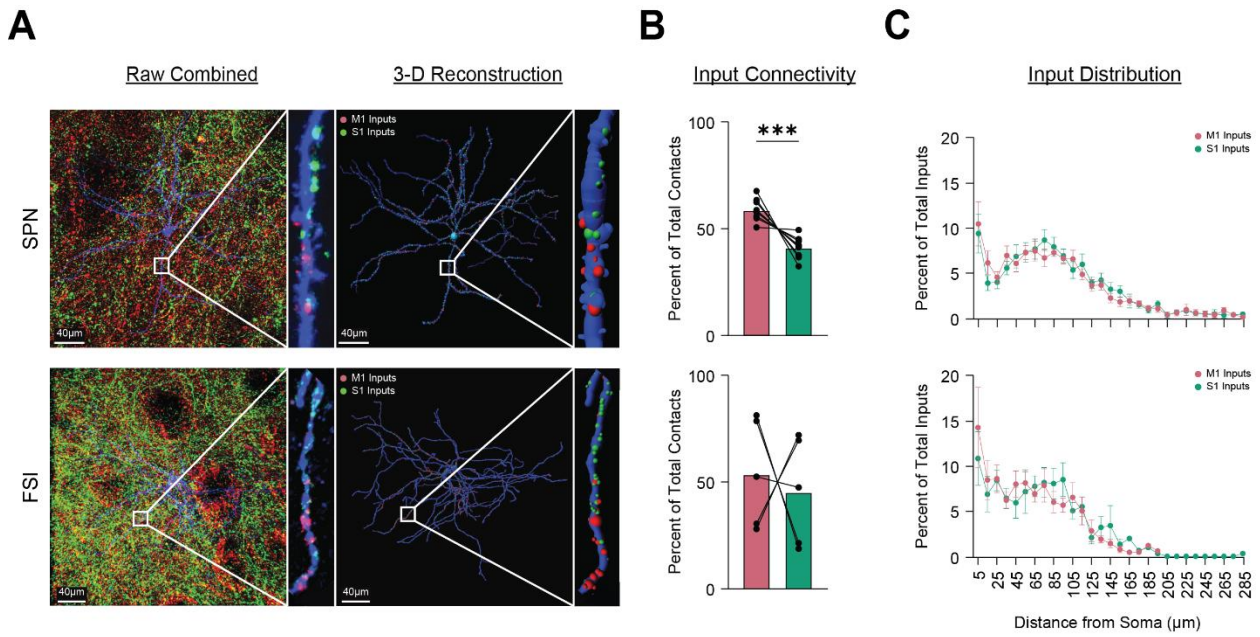

bioRxiv preprint doi: https://doi.org/10.1101/2023.03.06.531405; this version posted March 7, 2023. The copyright holder for this preprint (which was not certified by peer review) is the author/funder, who has granted bioRxiv a license to display the preprint in perpetuity. It is made available under aCC-BY-NC 4.0 International license.

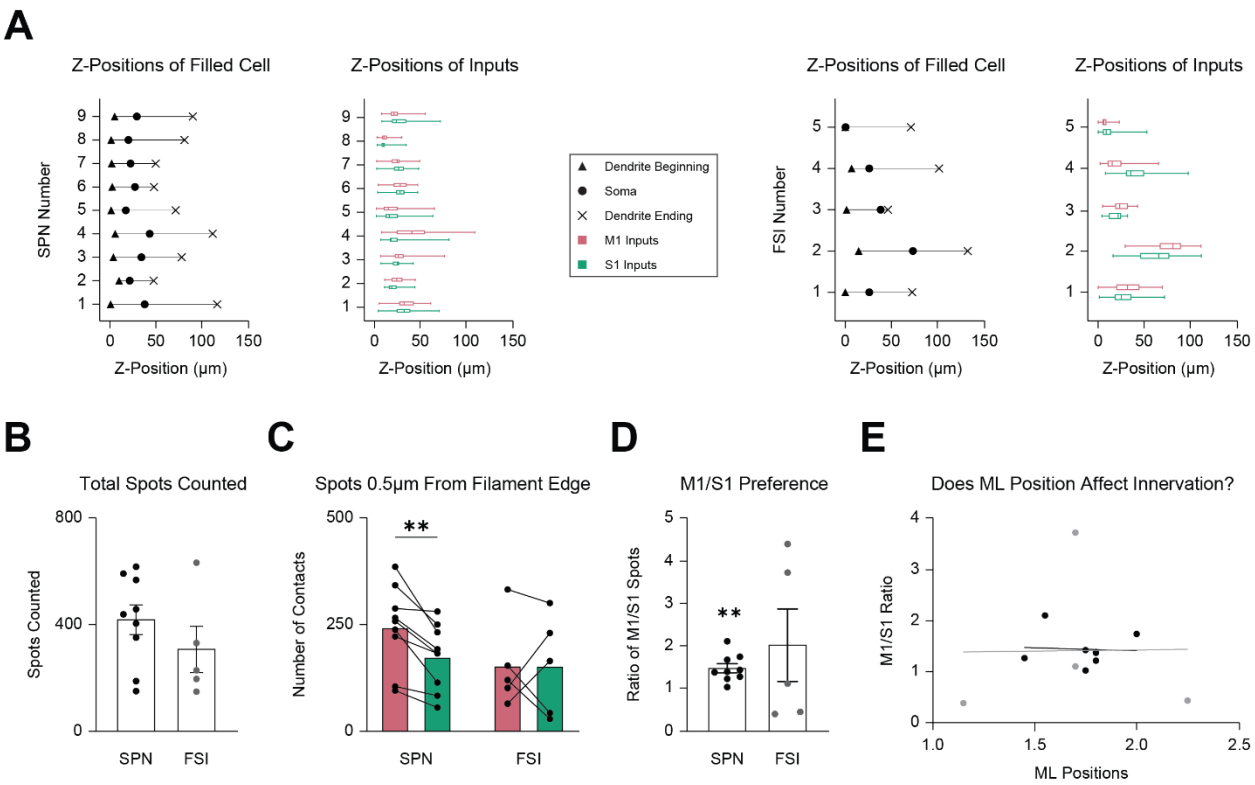

bioRxiv preprint doi: https://doi.org/10.1101/2023.03.06.531405; this version posted March 7, 2023. The copyright holder for this preprint (which was not certified by peer review) is the author/funder, who has granted bioRxiv a license to display the preprint in perpetuity. It is made available under aCC-BY-NC 4.0 International license.